



Structure and mechanical properties of reactive and non-reactive sputter deposited WC based coatings



T. Glechner^{a,*}, R. Hahn^a, L. Zauner^a, S. Rißlegger^a, A. Kirnbauer^a, P. Polcik^b, H. Riedl^a

^a Institute of Materials Science and Technology, TU Wien, A-1060 Wien, Austria

^b Plansee Composite Materials GmbH, D-86983 Lechbruck am See, Germany

ARTICLE INFO

Article history:

Received 18 May 2021

Received in revised form 25 June 2021

Accepted 9 July 2021

Available online 13 July 2021

Keywords:

Thin films

Magnetron sputtering

Crystal structure

Tungsten carbide

Carbon bonding

ABSTRACT

During the growth of WC based thin films, carbon can be introduced by either a non-reactive or reactive deposition route. In this study, we compare the influence of the carbon origin on the coating properties, sputtering three different target materials – a ceramic WC, a ceramic WC including a conventional cobalt binder, and a metallic tungsten (W) target – in reactive (acetylene, C₂H₂) as well as non-reactive (pure Ar) atmospheres. The morphology changes, independently to the target type and atmosphere used, from crystalline (*hex*-W₂C rich to pure *fcc*-WC_x) to a nanocomposite (*fcc*-WC_x nanometre sized grains embedded in an amorphous matrix) structure, up to amorphous coatings, only dominated by the prevalent C/W ratio. The cobalt binder however leads to a preferred amorphization of the coatings. The highest hardness is obtained for predominantly *fcc* structured WC_{0.67} (WC ceramic target), $H = 40 \pm 1.7$ GPa, exhibiting also an excellent intrinsic fracture toughness of $K_{IC} = 3.3 \pm 0.33$ MPa·m^{1/2} obtained by micro-mechanical testing. Furthermore, the bonding nature of carbon is distinctly affected by the reactive carbon source, leading to more pronounced π -bonded carbon peak with increasing C₂H₂/Ar flow rates.

© 2021 The Authors. Published by Elsevier B.V.
CC BY 4.0

1. Introduction

Transition metal carbide (TMC) based coating materials are known for their outstanding properties including high hardness, high thermal stability [1], excellent wear resistance, chemical inertness, and low coefficients of friction [2]. Among this class of thin films, tungsten carbide (WC) is well-established and has attracted much interest in the form of WC based Diamond-like-Carbon (DLC) coatings [2,3]. These coatings consist of nanocrystalline WC_x embedded in an amorphous carbon matrix, thereby having the advantage of low compressive stresses, while providing inherently low friction coefficients comparable to pure DLC coatings [2]. In literature, many deposition strategies are reported for the growth of these WC/DLC concepts, applying different target configurations – i.e. combinations of W [3–7], WC [8], WC+Co [9,10], or C [11] – sputtered in reactive (C₂H₂ or CH₄) and non-reactive (Ar) atmospheres. The different deposition approaches result in thin films consisting of various crystalline tungsten carbide-based phases next to a varying amount of additional amorphous carbon. Typically, the observed phases are *bcc*-tungsten, several modifications of W₂C (SG 162, 60,

194 [12]), metastable *fcc*-WC_x [9], and *hex*-WC (SG 187, [13]). When attempting to deposit single-phased WC_x – without an additional amorphous carbon phase – often a mixture of *fcc*-WC_x and W₂C is observed [8,11]. Recently, a study [14] highlighted the stabilization of *fcc*-WC_x by C vacancies, being in good relation to other *fcc* structured TMC based coating materials and their tendency to be carbon deficient [15,16]. During the sputter deposition of transition-metal (TM) carbides the microstructure typically transforms from a single phased structure – most likely a sub-stoichiometric carbide – to a nanocomposite microstructure with increasing carbon content, which eventually leads to TMC_x nanoclusters embedded in amorphous carbon [17]. This evolution is observed independently to the gas mixture used during sputtering, whether a reactive or non-reactive source provides the carbon. However, for DLC coatings it is reported that the carbon source (reactive gas or graphite target) influences the carbon hybridization, leading to tetrahedral amorphous carbon (ta-C), amorphous carbon (a-C), and hydrogenated amorphous carbon (a-C:H) DLC coatings, which differ by altered ratios of sp² to sp³ hybridized C–C bonds [18]. However, a direct comparison between non-reactive and reactive sputter deposited WC_x films correlating the bonding states and morphology with the mechanical properties is still missing. Furthermore, transition metal carbides typically exhibit a low fracture tolerance, being a limiting factor for many applications [19]. Several strategies [20] have been

* Corresponding author.

E-mail address: thomas.glechner@tuwien.ac.at (T. Glechner).

established to enhance the fracture toughness of TMC based thin films, i.e. nitrogen alloying to form TM-carbonitrides [21]. This approach was experimentally found to be highly effective for the Ta-C-N [22,23] system and further underlined in a study on Hf-C-N, where the theoretically proposed [21] dependency between ductility and valence electron concentration (VEC) was confirmed [24]. According to this latter work, the fracture toughness of WC (VEC = 10) should be even higher compared to e.g. TaC_{0.64}N_{0.36} (VEC = 9.36). Moreover, the influence of the film morphology on the fracture toughness and especially crack pathways is still a pending topic for coating materials in general.

Therefore, in this study, we compare the three most commonly used target types to deposit tungsten carbide based thin films: (i) a ceramic WC target, (ii) a ceramic WC including a conventional cobalt binder, and (iii) a metallic tungsten (W) target, sputtered in both non-reactive and reactive atmospheres, respectively. The differences between these targets are elaborated with respect to the microstructure, mechanical properties, and carbon bonding states with a focus also on fracture behavior.

2. Experimental details

For the deposition of all tungsten carbide containing thin films, an in-house built magnetron sputtering system (FRIDA) was used. In the course of this study, the system was equipped with three different targets: (i) a ceramic WC target, (ii) a ceramic WC including a conventional cobalt binder, and (iii) a metallic tungsten (W) target (3-inch sized, Plansee Composite Materials GmbH). All coatings were deposited in DC mode using either a pure argon atmosphere or an argon/acetylene mixture, respectively. The working pressure was controlled by the gas flow maintained at 40 sccm in total. Depending on the acetylene to total gas flow ratio ($f_{[C_2H_2]}^{norm} = \frac{f_{C_2H_2}}{f_{C_2H_2} + f_{Ar}} \cdot 100\%$) this resulted in a deposition pressure of $p = 0.42\text{--}0.36$ Pa. The target and substrate holder were aligned parallel at a distance of 73 mm using no substrate heating. All depositions were conducted at a target current of 0.75 A, while keeping the substrate bias at floating potential (approx. -20 V). In the Appendix, an overview on additional depositions is included, where also the working gas pressure, the target current, and the substrate bias potential was varied, respectively.

All thin films were deposited on polished austenitic stainless-steel platelets ($20 \times 7 \times 0.8$ mm³) and polished single crystalline Si samples (100-oriented, $20 \times 7 \times 0.38$ mm³). Prior to each deposition, the substrates were cleaned in an ultrasonic bath by means of acetone and ethanol for 5 min each, respectively. Furthermore, both the targets and the substrates were sputter-cleaned in a pure argon atmosphere (180 sccm, 5 Pa, 500 V) right before the deposition.

To determine the crystalline structure of the deposited thin films, X-ray diffraction (XRD) was used in Bragg Brentano configuration on a Panalytical Empyrean diffractometer equipped with a Cu-K_α radiation source (wavelength $\lambda = 1.5418$ Å). The mechanical properties, such as hardness (H) and Young's modulus (E), were determined on austenitic steel substrates by means of nanoindentation. The Ultra-Micro-Indentation System (UMIS) was equipped with a Berkovich diamond tip. For every sample, 30 indents with different loads (3–45 mN) were performed and subsequently, the recorded load-displacement curves were analyzed according to Oliver and Pharr [1]. For the Young's modulus, an extrapolation to zero indentation depth was performed to minimize the substrate influence (using the power-law function $y = a \cdot (1 + x)^b$ [25], where a is the given modulus).

Investigations on the film morphology were realized using a transmission electron microscope (TEM FEI TECNAI G20, acceleration voltage of 200 kV). Furthermore, electron energy-loss spectroscopy (EELS) was carried out to describe the bonding states of the deposited films. The core-loss edges were recorded with a 2 mm

entrance aperture (dispersion 0.3 eV/pixel). The effect of plural scattering was removed by deconvolution with the low loss spectra. To exclude the influence of environmental carbon on the energy loss near edge structures (ELNES), all samples were He-plasma cleaned directly before performing the TEM analysis.

X-ray photoelectron spectroscopy (XPS) spectra were recorded using a custom-built SPECS XPS-spectrometer equipped with a monochromatic Al-K_α X-ray source (μ Focus 350, spot size = 450 μ m, power = 70 W) and a hemispherical WAL-150 analyzer (acceptance angle of 60°). Overview, as well as detailed spectra of the single elements, were measured with pass-energies of 100 and 30 eV and an energy resolution of 1 eV and 100 meV, respectively. To minimize surface contaminations, Ar-ion etching was carried out for 100 s at a total pressure of $2 \cdot 10^{-7}$ mbar applying a voltage of -3.0 kV. The spectrum analysis was conducted using transmission corrections (as per manufacturer's specifications), Shirley-backgrounds, and sensitivity parameters after Scofield [26]. For charge correction, the binding energy value of adventitious carbon, based on minor surface contamination, was set to 284.8 eV.

The fracture toughness was calculated according to Matoy et al. [27]:

$$K_{IC} = \frac{P_{max} \cdot l}{b \cdot w^{\frac{3}{2}}} f\left(\frac{a}{w}\right) \quad (1)$$

with

$$f\left(\frac{a}{w}\right) = 1.46 + 24.36 \cdot \left(\frac{a}{w}\right) - 47.21 \cdot \left(\frac{a}{w}\right)^2 + 75.18 \cdot \left(\frac{a}{w}\right)^3$$

Where P_{max} is the maximum fracture force, w is the height of the cantilever, b is the width of the cantilever, and l is the length between the initial crack and the indenter tip. The depth of the incipient crack is denoted as a . The dimensions of the microcantilever, as well as the crack initiation, were made by considering the findings of Brinckmann et al. [28,29].

The cantilevers are milled in a ThermoFisher Scios2 dual-beam FIB, and care was taken to correct any angles deviating from 90° by tilting the sample accordingly. We ensured that the device is well focused and shows as little astigmatism as possible when the initial notch is milled. The beam current for forming the cantilever was set to 1 nA, the initial was made with 50 pA to minimize possible influence by Ga⁺ ions. Before milling, the Si substrate was removed by SF₆ plasma etching to obtain free-standing film material.

The beam was tested with an intrinsically displacement-controlled FemtoTools FT-NMT04, equipped with a diamond wedge tip, at a loading rate of 10 nm·s⁻¹. During the test, this device was placed in a FEI Quanta 250 FEGSEM, which was also used to measure the fracture surface geometries required for the calculation.

3. Results and discussion

To gain a detailed insight on the sputter behavior of each target material, the poisoning trend of all three target types was studied with respect to an increasing acetylene flow-rate ratio. The acetylene to total gas flow ratio ($f_{[C_2H_2]}^{norm}$) was varied between 0% and 60% (corresponding to $p = 0.42\text{--}0.3$ Pa) using a constant target current of 0.75 A at a total gas flow of 40 sccm. The ceramic WC target increases in power density from 7.7 (pure argon) up to 9.1 W/cm² for $f_{[C_2H_2]}^{norm} = 30\%$, followed by a decrease down to 7.9 W/cm² for $f_{[C_2H_2]}^{norm} = 60\%$. Moreover, a small hysteresis effect can be observed between $f_{[C_2H_2]}^{norm} = 25\%$ and 55%. The cobalt binder containing WC target shows a very similar behavior, with slightly higher power densities throughout the entire acetylene flow range investigated. Finally, the metallic tungsten target starts at a target power density of 7.0 W/cm² for $f_{[C_2H_2]}^{norm} = 5\%$ and exhibits a maximum at $f_{[C_2H_2]}^{norm} = 40\%$ (corresponds to 8.9 W/cm²). At higher values of $f_{[C_2H_2]}^{norm} > 45\%$ the poisoned W behaves

similar as its ceramic counterparts. The two ceramic based target materials exhibit a deposition rate of around 65 nm/min in pure argon atmosphere, being slightly increased to 80 nm/min at 5% acetylene. At higher $f_{[C_2H_2]}^{norm}$ ratios the deposition rate decreases again down to 60 nm/min ($f_{[C_2H_2]}^{norm} = 25\%$). For the metallic tungsten target, the deposition rate is around 65 nm/min at $f_{[C_2H_2]}^{norm} = 5\%$, and increases to 80 nm/min at 10%, followed by a decrease for even higher $f_{[C_2H_2]}^{norm}$. With a deposition time of 40 min the total thickness of the coatings ranged between 2.4 and 3.2 μm .

In relation to the observed poisoning behavior, the acetylene flow-rate ratio was varied for all three target materials up to $f_{[C_2H_2]}^{norm} = 25\%$, respectively. In Fig. 1, the chemical compositions determined by XPS are summarized for all coatings deposited. The carbon to tungsten ratio (C/W) is plotted as a function of the acetylene to total gas flow ratio ($f_{[C_2H_2]}^{norm}$) and the target type used. With increasing acetylene flow-rate ratio, C/W increases for all three target types even with a similar slope. Apart from the initial differences in carbon content the alike slopes suggest, that the amount of additional carbon uptake into the film structure, due to an increasing fraction of acetylene in the chamber, remains basically unaffected by the target type used. This is in good agreement to the study of Bewilogua et al., where the W/C ratios of both a metallic tungsten and a ceramic WC target were compared for high acetylene flow rates [2]. Simultaneously, the cobalt content within the coatings deposited from the ceramic target including a cobalt binder decreases from 7 at% in pure argon atmosphere, down to 3.5 at% for $f_{[C_2H_2]}^{norm} = 25\%$. Interestingly, these films also exhibit a lower C/W ratio when sputtered in pure Argon atmosphere than thin films grown with the ceramic WC target under the same conditions.

Based on literature [5,6,8,17], the morphology of transition metal carbide based coatings strongly correlates with the carbon content present during film growth, starting with predominantly crystalline structures for sub-stoichiometric compositions changing to nanocomposites, and eventually to fully amorphous thin film materials with an increasing amount of carbon. Especially, when sputtering tungsten carbide-based coatings, also different crystal structures are known to compete. Hence, in the following the impact of the target type on these two properties – structure and morphology – will be discussed from the aspect of an increasing $f_{[C_2H_2]}^{norm}$.

In Fig. 2, the crystal structure determined by XRD is shown for all three target types, with the individual diffractograms grouped into the corresponding subcategories and sorted by an increasing acetylene flow rate ratio from top to bottom. With an increasing amount

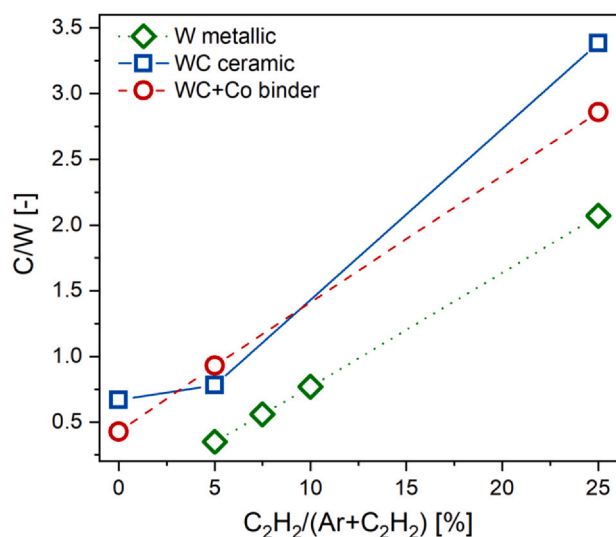


Fig. 1. Impact of the acetylene concentration in the working gas on the carbon to tungsten (C/W) ratio in the thin films determined by XPS.

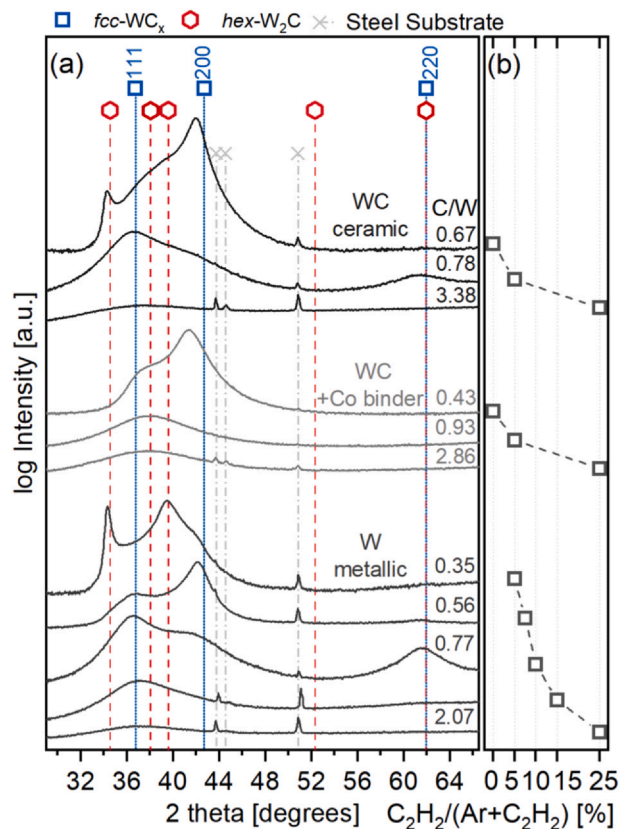


Fig. 2. (a) Structural evolution of WC_x coatings prepared from three different target types (WC ceramic, WC ceramic including a cobalt binder, and metallic tungsten) as a function of $f_{[C_2H_2]}^{norm}$. Diffractograms corresponding to the same target material are grouped accordingly, with an increasing C/W ratio from top to bottom. [30,31] (b) C_2H_2 flow rate ratios given in percent for all coatings shown in (a), corresponding data sets are horizontally aligned.

of acetylene present, the coatings for each target shift from a predominantly crystalline to an amorphous structure, where only a small hump in the spectrum remains. Yet, the amount of acetylene necessary to induce this transition is individual for each target. Thin films deposited from the ceramic WC target initially ($f_{[C_2H_2]}^{norm} = 0$) exhibit a mixture of $fcc-WC_x$ and $hex-W_2C$ [30,31] at a C/W ratio of 0.67. At only $f_{[C_2H_2]}^{norm} = 5\%$, the intensity of the crystalline diffraction peaks decreases drastically, whereby the $hex-W_2C$ related peaks disappear (a similar behavior was found in Ref. [8]). Regarding the Co containing WC target at $f_{[C_2H_2]}^{norm} = 5\%$, the thin film has already attained a completely amorphous state, which remains unchanged at higher acetylene flow rates. In pure argon atmosphere, this target yield to predominantly face-centered cubic structure at a C/W ratio of 0.43. Coatings deposited from the metallic tungsten target change from a $hex-W_2C$ (C/W=0.35) rich to a $fcc-WC_x$ dominated (C/W=0.56) to a fully amorphous structure with an increasing amount of acetylene. Finally, at $f_{[C_2H_2]}^{norm} = 25\%$ all thin films are X-ray amorphous. Furthermore, for all coatings the (200) diffraction peak of the $fcc-WC_x$ phase is shifted to lower 2 theta angles compared to the reference positions obtained from [30,31].

Complementary, selected area electron diffraction (SAED) analysis (see Figs. 3 and 4, left column) confirm the structures observed by XRD. Blue dashed lines correspond to the $fcc-WC_x$ phase, whereas red dotted lines indicate the $hex-W_2C$ phase. Resulting from the minute distances between the diffraction spots of the hexagonal and the face-centered-cubic structures, it was not possible to determine the actual content of $fcc-WC_x$ and $hex-W_2C$ phases, neither by XRD nor by SAED. The corresponding bright field images are shown in Figs. 3 and 4 (see right columns) revealing the direct relation

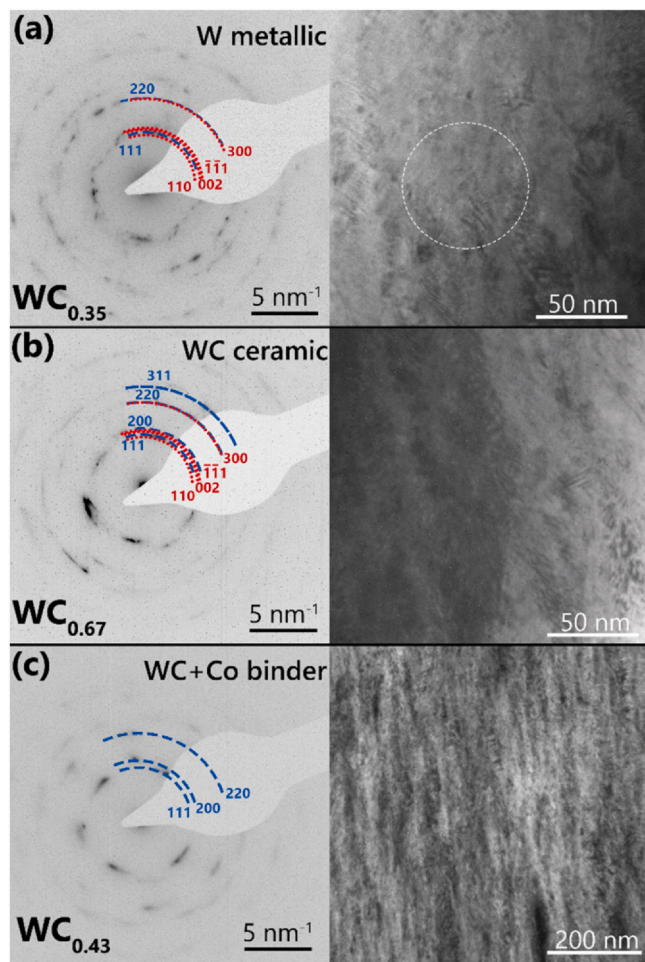


Fig. 3. SAED (left column) and bright field images (right column) of thin films with crystalline morphology determined by TEM. (a) Thin film prepared from a metallic tungsten target sputtered with $f_{[C_2H_2]}^{norm} = 5\%$. Thin films synthesized from (b) a WC ceramic and (c) a WC ceramic + cobalt binder target, respectively, both operated in pure argon atmosphere. In the SAED images, blue dashed lines correspond to *fcc*-WC_x, whereas red dashed lines denote *hex*-W₂C.

between the diffraction patterns obtained by SEAD and XRD and the film morphology. From these morphologies observed in TEM, three distinct classifications were identified for all samples: predominantly crystalline, nanocomposite, and amorphous. The crystalline structures (varying amount of *fcc*-WC_x and *hex*-W₂C) are obtained only when operating the ceramic targets in pure argon atmosphere – ceramic WC (WC_{0.67}, see Fig. 3b) and ceramic WC + Co binder (WC_{0.43}, see Fig. 3c) – as well as for $f_{[C_2H_2]}^{norm} = 5\%$ and 7.5% on the metallic tungsten target ($f_{[C_2H_2]}^{norm} = 5\%$, WC_{0.35}, see Fig. 3a). The crystalline thin films exhibit dense columnar grains, with a mean grain size of around 30 nm for both WC_{0.67} and WC_{0.35} (see Fig. 3a and b), and 25 nm for WC_{0.43} (see Fig. 3c). Here it should be mentioned, that for the latter WC_{0.43} coating, obtained from the Co containing WC target, the substrate near region shows an amorphous structure, which transform to a more crystalline morphology during the growth process. We relate this effect to an increasing substrate temperature during the deposition process, as a result of the kinetic energy of the impinging Ar⁺ ions and the arriving film flux. Fig. 4 shows thin films with a nanocomposite (see Fig. 4a and b) and an amorphous (see Fig. 4c) morphology. The nanocomposite film structure was observed for coatings deposited from metallic tungsten (WC_{0.77}, see Fig. 4a) and the ceramic WC target (WC_{0.78}, see Fig. 4b) at $f_{[C_2H_2]}^{norm} = 10\%$ and 5%, respectively. These thin films exhibit small grains (only a few nanometres in diameter) embedded in an

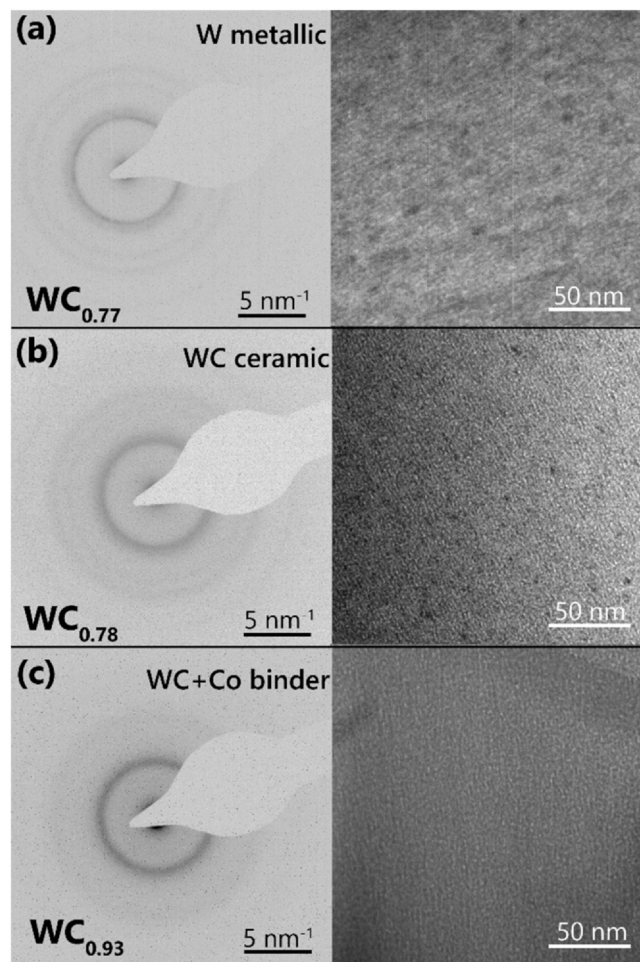


Fig. 4. SAED (left column) and bright field images (right column) of thin films with nanocomposite/amorphous morphology determined by TEM. (a) Thin film deposited using a metallic tungsten target sputtered with $f_{[C_2H_2]}^{norm} = 10\%$. Thin films synthesized with a WC ceramic (b) and WC ceramic + cobalt binder target (c) sputtered with $f_{[C_2H_2]}^{norm} = 5\%$.

amorphous matrix. Moreover, the SAED patterns present no distinct spots, but rather exhibit blurry but continuous diffraction rings, being a good indication for the very small and randomly oriented grains. In accordance with the XRD analysis for WC_{0.77} (see Figs. 2a and 4a), the SAED image shows slightly more pronounced diffraction rings (i.e. peaks in the XRD spectrum) than for the WC_{0.78} (see Fig. 4b) coating, which suggests larger grains for the WC_{0.77} sample. Fig. 4c shows the thin film deposited using the WC + Co binder target with an acetylene flow rate ratio of $f_{[C_2H_2]}^{norm} = 5\%$. Here, the thin film already grows in a completely amorphous structure indicated by the flat/amorphous XRD pattern (see Fig. 2a) as well as the bright field image (see Fig. 4c, right column). Along with the observations made in pure argon atmosphere, this indicates that the additional cobalt in the target significantly affects the crystallization of tungsten carbide and promotes the amorphization of the thin films when compared to the pure ceramic WC target without any binder.

Summarizing the evolution of structure and morphology, with increasing $f_{[C_2H_2]}^{norm}$ and thus C/W ratio, the WC_x based thin films show a transition from *hex*-W₂C rich, to mixed, predominantly *fcc*-WC_x structured coatings in the crystalline regime ($C/W < \sim 0.77$). With increasing $f_{[C_2H_2]}^{norm}$ the crystalline *fcc*-WC_x phase with a preferred (200)-texture transforms into a nanocomposite morphology comprised of nanometer sized *fcc*-WC_x grains embedded in an amorphous matrix. When further increasing $f_{[C_2H_2]}^{norm}$, all thin films eventually obtain a completely amorphous growth. However, when

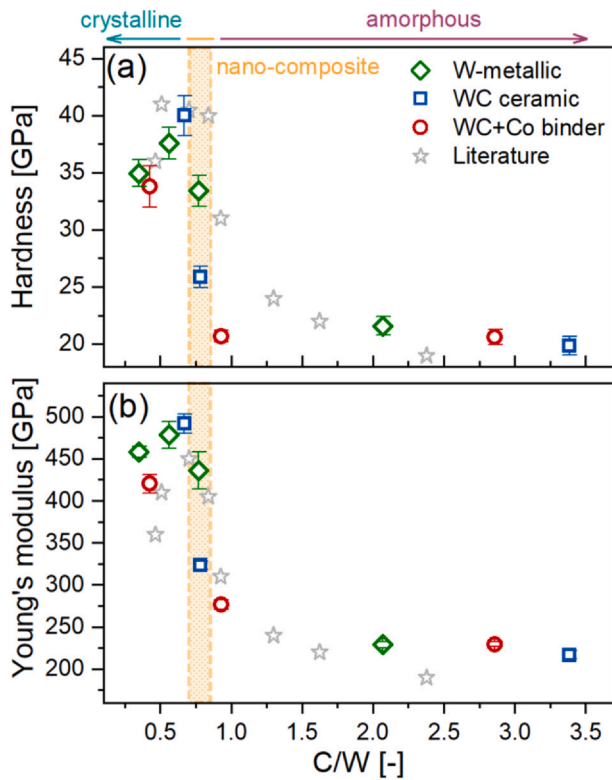


Fig. 5. (a) Hardness and (b) Young's modulus evolution as a function of an increasing C/W ratio for all WC_x coatings prepared from the three different target types. The three morphological coating regimes, i.e. crystalline, nanocomposite, and amorphous, are additionally indicated. Values from Ref. [6] (metallic tungsten target and acetylene containing working gas) are indicated as grey stars.

using the ceramic WC target including a Co binder no nanocomposite morphology was observed. Interestingly, the C/W ratio indicating the transition from a crystalline to a nanocomposite coating at around 0.77 is very similar for both the metallic tungsten and ceramic WC target materials. In addition, this carbon content of 43 at% corresponds well with the content reported in Refs. [6,18,19] for the transition from a crystalline to a nanocomposite morphology.

Furthermore, we studied the influence of $f_{[C_2H_2]}^{norm}$ and hence the structure and morphology on the hardness and Young's modulus of all deposited WC_x based coatings. For a better comparison of the results between the different target types investigated, Fig. 5a and b show all hardness and Young's modulus data points plotted versus a common C/W ratio axis. The plot is additionally divided into 3 regions depending on the morphology type of the resulting films: crystalline ($C/W < 0.77$), nanocomposite ($0.77 < C/W < 0.85$), and amorphous ($C/W > 0.85$). In the crystalline region, the thin films expectably exhibit the highest hardness with values ranging between 34 and 40 GPa. The highest hardness of 40 ± 1.7 GPa was obtained for $WC_{0.67}$ deposited from the pure ceramic WC target. The hardness noticeably decreases in the nanocomposite regime and settles at around 20 GPa for the amorphous thin films. Furthermore, for a complete interpretation of the data, it is important to consider that the crystalline thin films exhibit different phases, being *fcc*- WC_x , *hex*- W_2C , or a mixture of both. Moreover, the different target types lead to individual phase compositions for the same C/W ratio, which restricts a direct comparison of the data presented in Fig. 5. However, when neglecting the C/W ratio and merely taking the film structure into account, the trend in hardness suggests that the hardness increases from *hex*- W_2C rich to *fcc*- WC_x structured coatings, yet exhibiting a maximum with a low amount of *hex*- W_2C phase, and then decreases with increasing amorphous fractions. The Young's modulus follows a similar trend line as the hardness starting

at values between 450 and 500 GPa for the crystalline states, and subsequently decreases to around 200 GPa for the fully amorphous coatings. Overall, these trends in film hardness fit very well to trends from previous studies [6,32,33] where metallic tungsten or ceramic WC targets were utilized. Additional deposition parameter variations conducted for the WC ceramic target showed that both the structure and the mechanical properties are quite stable throughout variations in pure argon atmosphere. However, for $f_{[C_2H_2]}^{norm} = 5\%$, with the morphology situated inside the nanocomposite range, the mechanical properties are increasingly sensitive towards changes in deposition conditions. Further details are shown in the Appendix. We, therefore, conclude that the nanocomposite morphology is quite sensitive to parameter variations – hence changing of the growth conditions e.g. adatom mobility at the surface – and can lead to considerable changes of the mechanical properties. In addition, adhesion test after [34] highlighted, that crystalline coatings obtaining a dual phase structure tend to have worse adhesion to the used steel substrates compared to the amorphous and nano-composite coatings.

Apart from hardness and Young's modulus, the fracture toughness is an important mechanical property for TM-carbides, since a low tolerance against crack propagation can be a major limiting factor for the applicability of such coatings. The fracture toughness was determined by microcantilever beam-bending tests of the thin films deposited using the pure WC ceramic target. The three tested coatings, $WC_{0.67}$, $WC_{0.78}$, and $WC_{3.38}$, comprise distinctly different morphologies from the three regimes identified, crystalline, nanocomposite, and amorphous respectively – see also Figs. 3,4, and 5. Fig. 6 shows representative load-displacement curves and the fracture cross-sections of all samples tested, including a microcantilever beam in the as-prepared state. The determined fracture toughness

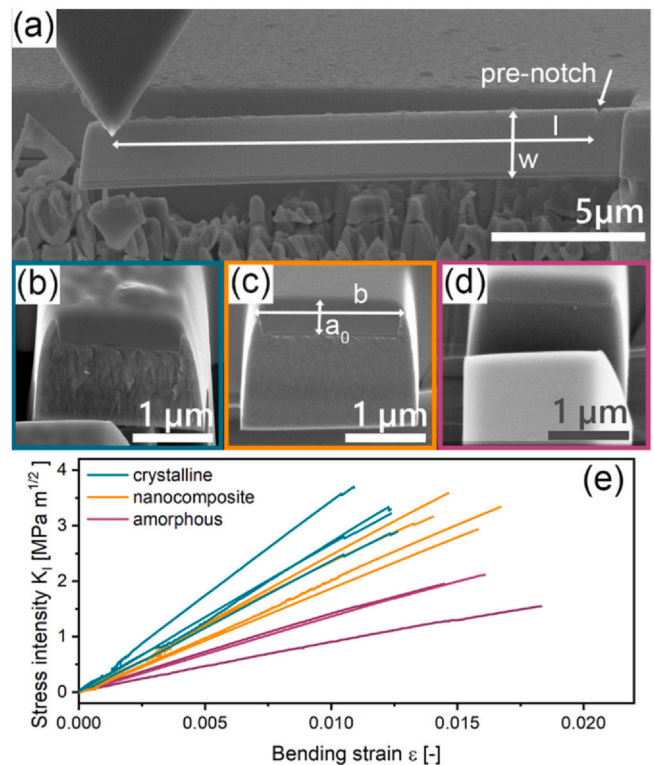


Fig. 6. Microcantilever beam-bending test of coatings deposited using a pure ceramic WC target. (a) Representative SEM image of a microcantilever beam in the as-prepared state, indicating the position of the pre-notch as well as the nanoindenter wedge tip. Post-mortem SEM fracture cross-sectional image of the (b) crystalline $WC_{0.67}$, (c) nanocomposite structured $WC_{0.78}$, and (d) amorphous structured $WC_{3.38}$ cantilever beam samples. Representative load-displacement curves corresponding to the WC_x coatings are shown in (e).

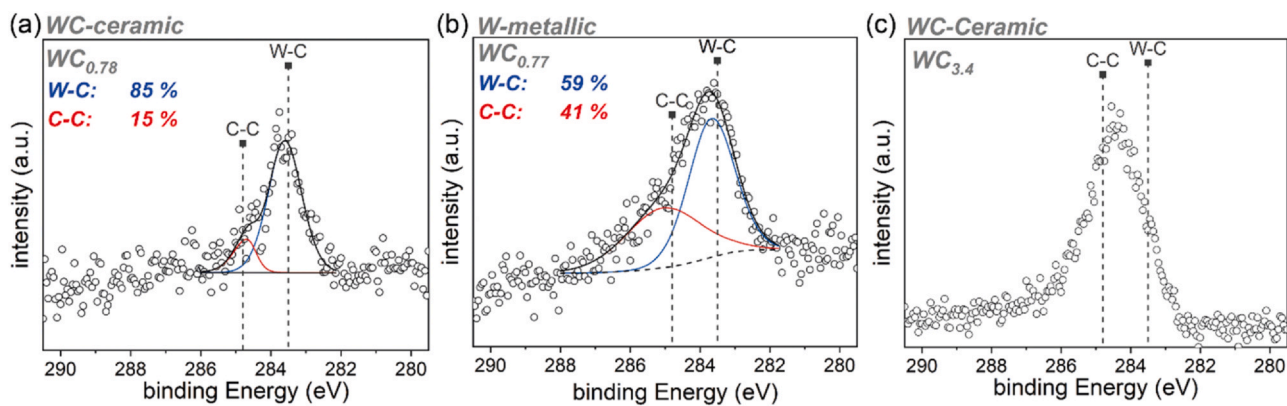


Fig. 7. Selected XPS spectra of WC_x coatings deposited with the WC ceramic (a,c) and metallic tungsten target (b). The vertical reference lines indicate the peak positions of carbon that is bonded to tungsten (283.5 eV) and to another carbon atom (284.8 eV).

values K_{IC} are $3.3 \pm 0.33 \text{ MPa}\cdot\text{m}^{1/2}$ for WC_{0.67}, $3.2 \pm 0.24 \text{ MPa}\cdot\text{m}^{1/2}$ for WC_{0.78}, and $1.9 \pm 0.24 \text{ MPa}\cdot\text{m}^{1/2}$ for WC_{3.38} (4 beams tested for each coating). The high K_{IC} value observed for the crystalline WC_{0.67} is a further confirmation of the direct correlation between the VEC and the fracture toughness of TM-carbides and nitrides, as already proposed theoretically and experimentally [21,23,24,35]. In comparison, the K_{IC} values of group IV and V TM-carbides such as Hf-C and Ta-C are below $2 \text{ MPa}\cdot\text{m}^{1/2}$ [23,24]. Furthermore, it is astonishing that WC_{0.67} and WC_{0.78} exhibit very similar K_{IC} values despite having a drastically different morphology, which in turn suggest that the film growth characteristics only have a minor influence on the overall fracture resistance of these films. This is in line with Ref. [36] where the measured fracture toughness of Cr₂AlC coatings was only moderately affected by the microstructure. However, that study on the other hand reports an increased fracture toughness for amorphous Cr₂AlC. Therefore, the fact that the amorphous WC_{3.38} coating in this study exhibits a much lower K_{IC} value might be an indication that the type of atomic bonds is of vital importance. Therefore, we wanted to gain a closer insight into the bonding nature, especially on carbon in the different morphologies obtained from the three target types and $f_{[C_2H_2]}^{norm}$, respectively.

Fig. 7 shows selected C1s spectra obtained by XPS of thin films deposited from the ceramic WC and metallic tungsten target, respectively. In the spectra, carbon bonded to tungsten results in a peak at 283.5 eV [37], whereas C–C bonds result in a peak at 284.8 eV, as indicated by the vertical reference lines. For all targets the content of amorphous carbon (i.e. the amount of C–C bonds) increases with increasing $f_{[C_2H_2]}^{norm}$ – hence also C/W ratio – starting at around 15% at the lowest C/W ratio for each target. Fig. 7a and b compares thin films deposited using the ceramic WC target ($f_{[C_2H_2]}^{norm} = 5\%$, see Fig. 7a) to thin films deposited from the metallic tungsten target ($f_{[C_2H_2]}^{norm} = 10\%$, see Fig. 7b) with a similar C/W-ratio. Both exhibit a nanocomposite morphology but the ceramic WC target yields a much lower amount of amorphous carbon, with 15 versus 41% for the metallic tungsten target. Furthermore, the amount of amorphous carbon for a predominantly crystalline WC_{0.67} and nanocomposite WC_{0.78} (deposited using the WC ceramic target) coating is similar with, 21% and 15% C–C respectively. This suggests that the amorphous matrix in the nanocomposite morphology is not only comprised of amorphous carbon as proposed in literature [17] for TM-carbides in general, but also of amorphous WC. When increasing the acetylene concentration during deposition (e.g. for the WC_{3.4} coating deposited with the ceramic WC target see Fig. 7c), the C1s spectra of all targets exhibits a peak being located close to the C–C reference position. However, it was not possible to do a satisfactory fit with a C–C and W–C peak hence no content of amorphous carbon is given.

Carbon exhibits different hybridization states, sp^2 and sp^3 , which is known to alter the properties of DLC coatings, resulting in various types such as ta-C- and a-C(H)-type DLC [18]. A way to determine the carbon hybridization is detailed EELS analysis via TEM, investigating the energy loss near edge structure (ELNES) at the C1s (K edge) position at 285 eV and beyond. The main features observed in this fine structure are an intensity peak at 285 eV due to excitation of the π^* antibonding orbital as well as a step at 290 eV due to excitation of the σ^* states [18,38,39]. Eventually, these two features can then be used to determine the sp^2 fraction of the sample [18]. In general, ELNES mirrors the unoccupied Density Of States (DOS) of a compound above the Fermi level [40]. However, in the thin films prepared for this study, a mixture of tungsten carbide and amorphous carbon prevails, leading to an overlap of the DOS of WC [23] and sp^2 (graphite) as well as sp^3 (diamond) [41] hybridized amorphous carbon. Therefore, only a qualitative comparison of the ELNES results at the C1s (K edge) position, for coatings prepared from the three different target types, are considered within this study. The results for the different target types at various values of $f_{[C_2H_2]}^{norm}$ (top to bottom) are shown in Fig. 8.

Thin films deposited from the ceramic WC target and Co containing one, show a transition from a spectrum with a single, continuous step at about 285 eV, to spectra with a clear peak separation and lowering of the π^* peak at increasing C/W ratio, i.e. acetylene flow rate. A similar transition was observed for TiC by J.C. Sánchez-López et al. [42], where the additional carbon was provided through co-sputtering a graphite target. In contrast to that, thin films deposited from the metallic tungsten target show this separation already at the lowest C/W ratio (WC_{0.35}) realized for all depositions. These results suggest that carbon originating from a reactive gas source results in a change of the ELNES, and hence different bonding and/or valence states of the carbon atoms. Furthermore, J. Schwan et al. [43] report that the ratio of energetic ions to neutral species influences the amount of sp^3 hybridization when depositing DLC thin films. In our case, this ratio could be influenced by the addition of acetylene to the gaseous environment. Due to the high ionisation energy of carbon and the use of DC magnetron sputtering we expect no ionized carbon atoms originating from the ceramic targets. On the other hand, carbon atoms originating from the acetylene molecules in the plasma are more likely to be ionized and hence could be responsible for the change of the ELNES. Furthermore, C₂H₂ might not be completely split up into H and C ions and arrive as C-H clusters at the substrate surface and hence the additional hydrogen can affect the bonding. This might be the reason why more amorphous carbon is found in the coatings using the metallic tungsten target. However, no further experiments were conducted to

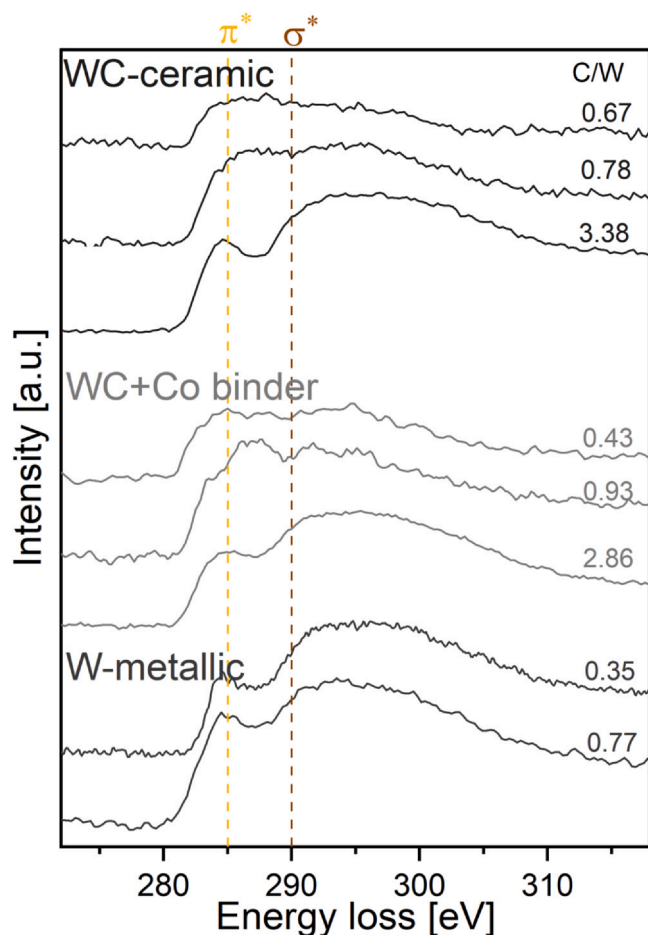


Fig. 8. Energy loss near edge structure (ELNES) at the C1s (K edge) position for coatings synthesized from all three target types, with increasing C/W ratio from top to bottom. The dashed lines mark the π^* peak at 285 eV and the σ^* step at 290 eV.

underline this explanation. Although the reason could not be fully answered within this study, we can conclude that the carbon bonds are significantly affected by the carbon source. Furthermore, no noticeable differences in the carbon bonding state of crystalline $WC_{0.67}$ and nanocomposite $WC_{0.78}$ could be observed applying XPS and ELNES. This promotes the interpretation stated above, that the similar K_{IC} values of these two coatings ($WC_{0.67}$, $WC_{0.78}$) are mainly determined by the bonding nature and not the morphology. However, if the amorphous phase is predominated by C–C bonds, e.g. for the $WC_{3.38}$, a direct correlation between the fracture characteristics and the VEC is not valid any more.

4. Conclusion

In this study, we compare the influence of the carbon origin on the composition, structure, morphology, mechanical properties, as

well as bonding nature of sputter deposited WC_x coatings using three different target materials in reactive and non-reactive atmospheres. For the depositions a ceramic WC, a ceramic WC including a cobalt binder, as well as a metallic tungsten (W) target were utilized. Regardless to the target type used, the addition of acetylene increases the C/W ratio in all coatings linearly. Furthermore, the film structure and morphology changes from a crystalline structure (i.e. $hex-W_2C$ rich or pure $fcc-WC_x$) to a nanocomposite (i.e. phase-pure $fcc-WC_x$ nanometre sized grains in an amorphous matrix) up to a fully amorphous thin film, with increasing C/W ratio. However, the cobalt binder within the ceramic WC target material accelerates the amorphization of the coating morphology. The maximum hardness of $H = 40 \pm 1.7$ GPa was determined for predominantly fcc structured $WC_{0.67}$ containing also minor fractions of $hex-W_2C$. An increase of the C/W ratio lead for all target types to fully amorphous films obtaining hardness values around 20 GPa. The crystalline $WC_{0.67}$ coating exhibits a high fracture toughness ($K_{IC} = 3.3 \pm 0.33$ MPa·m^{1/2}) being in good agreement with the predicted VEC dependency of the fracture characteristics – suggesting VEC up to 10 being highly beneficial for crystalline coating materials. The bonding nature of carbon is distinctly affected by reactive carbon supply leading to more pronounced π -bonded carbon peak with increasing acetylene flow rates, especially when entering the amorphous regime.

In summary, the combination of different target materials in reactive and non-reactive atmospheres allows for a broad variation of the morphology and bonding nature, hence being a versatile tool to tune the mechanical properties of WC_x based coatings.

CRediT authorship contribution statement

T. Glechner: Conceptualization, Investigation, Writing – original draft. **L. Zauner:** Writing – review & editing. **R. Hahn:** Investigation. **S. Rißlegger:** Investigation. **A. Kirnbauer:** Investigation. **P. Polcik:** Resources, Conceptualization. **H. Riedl:** Supervision, Conceptualization, Writing – review & editing.

Declaration of Competing Interest

The authors declare that they have no known competing financial interests or personal relationships that could have appeared to influence the work reported in this paper.

Acknowledgments

We thank for the financial support of Plansee Composite Materials GmbH. In addition, we want to thank the X-ray center (XRC) of TU Wien for beam time as well as the electron microscopy center - USTEM TU Wien - for using the SEM and TEM facilities and the analytical instrumentation center – aic TU Wien – for using the XPS. We thank Dr. Simon Muntwyler from Femto Tools for the support with micromechanical testing. The authors acknowledge the TU Wien Bibliothek for financial support through its Open Access Funding Program.

Appendix

(See Fig. A1).

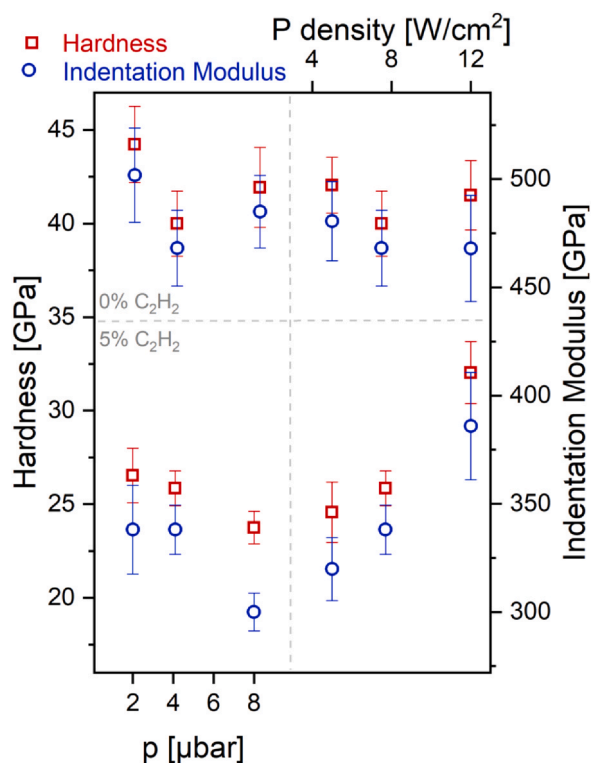


Fig. A1. Deposition parameter variations conducted in pure argon atmosphere (0% C_2H_2) for the ceramic WC target indicate that the structure and mechanical properties, shown in the upper part of the graph, remain rather unaffected. Hardness values range between 40 and 44 GPa with no clear correlation to the deposition pressure or the applied target power density. However, for $f_{[\text{C}_2\text{H}_2]}^{\text{nom}} = 5\%$ (i.e. nanocomposite structured WC_x coatings), the data shows a clear trend that lower deposition pressures or higher power densities lead to both higher hardness and indentation modulus.

References

- [1] H. Lasfargues, T. Glechner, C.M. Koller, V. Paneta, D. Primetzhofer, S. Kolozsvári, D. Holec, H. Riedl, P.H. Mayrhofer, Non-reactively sputtered ultra-high temperature Hf-C and Ta-C coatings, *Surf. Coat. Technol.* 309 (2017) 436–444.
- [2] K. Bewilogua, C.V. Cooper, C. Specht, J. Schröder, R. Wittorf, M. Grischke, Effect of target material on deposition and properties of metal-containing DLC (Me-DLC) coatings, *Surf. Coat. Technol.* 127 (2000) 223–231.
- [3] A.A. Voevodin, J.P. O'Neill, J.S. Zabinski, Tribological performance and tribochemistry of nanocrystalline WC/amorphous diamond-like carbon composites, *Thin Solid Films* 342 (1999) 194–200.
- [4] A.A. Voevodin, J.P. O'Neill, S.V. Prasad, J.S. Zabinski, Nanocrystalline WC and WC/a-C composite coatings produced from intersected plasma fluxes at low deposition temperatures, *J. Vac. Sci. Technol. A Vac. Surf. Films* 17 (1999) 986–992.
- [5] P. Gouypailler, Y. Pauleau, Tungsten and tungsten-carbon thin-films deposited by magnetron sputtering, *J. Vac. Sci. Technol. A Vac. Surf. Films* 11 (1993) 96–102.
- [6] A. Czyniewski, Deposition and some properties of nanocrystalline WC and nanocomposite WC/a-C: H coatings, *Thin Solid Films* 433 (2003) 180–185.
- [7] L. Wang, L. Li, X. Kuang, Effect of substrate bias on microstructure and mechanical properties of WC-DLC coatings deposited by HiPIMS, *Surf. Coat. Technol.* 352 (2018) 33–41.
- [8] K. Fuchs, P. Röddhammer, E. Bertel, F.P. Netzer, E. Gornik, Reactive and non-reactive high rate sputter deposition of Tungsten carbide, *Thin Solid Films* 151 (1987) 383–395.
- [9] E. Eser, R.E. Ogilvie, K.A. Taylor, The effect of bias on d.c. and r.f. sputtered WC-Co coatings, *Thin Solid Films* 67 (1980) 265–277.
- [10] A. Cavaleiro, M.T. Vieira, G. Lemperière, Structure and chemical composition of W-C-(Co) sputtered films, *Thin Solid Films* 197 (1991) 237–255.
- [11] M.A. Abad, M.A. Muñoz-Márquez, S.-El. El Mrabet, A. Justo, J.C. Sánchez-López, Tailored synthesis of nanostructured WC/a-C coatings by dual magnetron sputtering, *Surf. Coat. Technol.* 204 (2010) 3490–3500.
- [12] Y. Li, Y. Gao, B. Xiao, T. Min, Z. Fan, S. Ma, L. Xu, Theoretical study on the stability, elasticity, hardness and electronic structures of W-C binary compounds, *J. Alloy. Compd.* 502 (2010) 28–37.
- [13] E.C. Weigert, M.P. Humbert, Z.J. Mellinger, Q. Ren, T.P. Beebe, L. Bao, J.G. Chen, Physical vapor deposition synthesis of tungsten monocarbide (WC) thin films on different carbon substrates, *J. Vac. Sci. Technol. A* 26 (2008) 23–28.
- [14] P. Fang, B. Wang, C.P. Mulligan, T.M. Murray, S.V. Khare, D. Gall, Epitaxial growth of cubic WC (001) on MgO(001), *J. Alloy. Compd.* 860 (2021) 158403.
- [15] H. Li, S. Ma, L. Chen, Z. Yu, Carbon-deficient titanium carbide with highly enhanced hardness, *Front. Phys.* 8 (2020), <https://www.frontiersin.org/articles/10.3389/fphy.2020.00364/full?tag=makemoney0821-20>.
- [16] H. Riedl, T. Glechner, T. Wojcik, N. Koutná, S. Kolozsvári, V. Paneta, D. Holec, D. Primetzhofer, P.H. Mayrhofer, Influence of carbon deficiency on phase formation and thermal stability of super-hard TaC_y thin films, *Scr. Mater.* 149 (2018) 150–154.
- [17] U. Jansson, E. Lewin, Sputter deposition of transition-metal carbide films – a critical review from a chemical perspective, *Thin Solid Films* 536 (2013) 1–24.
- [18] J. Robertson, Diamond-like amorphous carbon, *Mater. Sci. Eng. R Rep.* 37 (2002) 129–281.
- [19] S. Kiani, J.-M. Yang, S. Kodambaka, Nanomechanics of refractory transition-metal carbides: a path to discovering plasticity in hard ceramics, *J. Am. Ceram. Soc.* 98 (2015) 2313–2323.
- [20] S. Fritze, P. Malinovsky, L. Riekehr, L. von Fieandt, E. Lewin, U. Jansson, Hard and crack resistant carbon supersaturated refractory nanostructured multi-component coatings, *Sci. Rep.* 8 (2018) 14508.
- [21] K. Balasubramanian, S.V. Khare, D. Gall, Valence electron concentration as an indicator for mechanical properties in rocksalt structure nitrides, carbides and carbonitrides, *Acta Mater.* 152 (2018) 175–185.
- [22] T. Glechner, P.H. Mayrhofer, D. Holec, S. Fritze, E. Lewin, V. Paneta, D. Primetzhofer, S. Kolozsvári, H. Riedl, Tuning structure and mechanical properties of Ta-C coatings by N-alloying and vacancy population, *Sci. Rep.* 8 (2018) 17669.
- [23] T. Glechner, R. Hahn, T. Wojcik, D. Holec, S. Kolozsvári, H. Zaid, S. Kodambaka, P.H. Mayrhofer, H. Riedl, Assessment of ductile character in superhard Ta-C-N thin films, *Acta Mater.* 179 (2019) 17–25.
- [24] T. Glechner, S. Lang, R. Hahn, M. Alfreider, V. Moraes, D. Primetzhofer, J. Ramm, S. Kolozsvári, D. Kiener, H. Riedl, Correlation between fracture characteristics and valence electron concentration of sputtered Hf-C-N based thin films, *Surf. Coat. Technol.* 399 (2020) 126212.
- [25] Y.-G. Jung, B.R. Lawn, M. Martyniuk, H. Huang, X.Z. Hu, Evaluation of elastic modulus and hardness of thin films by nanoindentation, *J. Mater. Res.* 19 (2004) 3076–3080.
- [26] J.H. Scofield, Hartree-Slater subshell photoionization cross-sections at 1254 and 1487 eV, *J. Electron Spectrosc. Relat. Phenom.* 8 (1976) 129–137.

- [27] K. Matoy, H. Schönherr, T. Detzel, T. Schöberl, R. Pippan, C. Motz, G. Dehm, A comparative micro-cantilever study of the mechanical behavior of silicon based passivation films, *Thin Solid Films* 518 (2009) 247–256.
- [28] S. Brinckmann, C. Kirchlechner, G. Dehm, Stress intensity factor dependence on anisotropy and geometry during micro-fracture experiments, *Scr. Mater.* 127 (2017) 76–78.
- [29] S. Brinckmann, K. Matoy, C. Kirchlechner, G. Dehm, On the influence of micro-cantilever pre-crack geometries on the apparent fracture toughness of brittle materials, *Acta Mater.* 136 (2017) 281–287.
- [30] International Center of Diffraction Data, Powder diffraction file 04–014-5679, 2019.
- [31] International Center of Diffraction Data, Powder diffraction file 04–022-5716, 2019.
- [32] B.R. Pujada, G.C.A.M. Janssen, Density, stress, hardness and reduced Young's modulus of W–C:H coatings, *Surf. Coat. Technol.* 201 (2006) 4284–4288.
- [33] K. Bewilogua, H. Dimigen, Preparation of W-C:H coatings by reactive magnetron sputtering, *Surf. Coat. Technol.* 61 (1993) 144–150.
- [34] N. Vidakis, A. Antoniadis, N. Bilalis, The VDI 3198 indentation test evaluation of a reliable qualitative control for layered compounds, *J. Mater. Process. Technol.* 143–144 (2003) 481–485.
- [35] S.-H. Jhi, J. Ihm, S.G. Louie, M.L. Cohen, Electronic mechanism of hardness enhancement in transition-metal carbonitrides, *Nature* 399 (1999) 132–134.
- [36] B. Völker, B. Stelzer, S. Mráz, H. Rueß, R. Sahu, C. Kirchlechner, G. Dehm, J.M. Schneider, On the fracture behavior of Cr₂AlC coatings, *Mater. Des.* 206 (2021) 109757.
- [37] K.L. Håkansson, H.I.P. Johansson, L.I. Johansson, High-resolution core-level study of hexagonal WC(0001), *Phys. Rev. B Condens. Matter* 49 (1994) 2035–2039.
- [38] J. Fink, T. Müller-Heinzerling, J. Pflüger, A. Bubenzer, P. Koidl, G. Crecelius, Structure and bonding of hydrocarbon plasma generated carbon films: an electron energy loss study, *Solid State Commun.* 47 (1983) 687–691.
- [39] H. Daniels, R. Brydson, B. Rand, A. Brown, Investigating carbonization and graphitization using electron energy loss spectroscopy (EELS) in the transmission electron microscope (TEM), *Philos. Mag.* 87 (2007) 4073–4092.
- [40] D.B. Williams, C.B. Carter, *Transmission Electron Microscopy: A Textbook for Materials Science*, Springer, 2009.
- [41] A. Snis, S.F. Matar, Electronic density of states, 1s core-level shifts, and core ionization energies of graphite, diamond, C₃N₄ phases, and graphitic C₁₁N₄, *Phys. Rev. B Condens. Matter* 60 (1999) 10855–10863.
- [42] J.C. Sánchez-López, D. Martínez-Martínez, Abad, A. Fernández, Metal carbide/amorphous C-based nanocomposite coatings for tribological applications, *Surf. Coat. Technol.* 204 (2009) 947–954.
- [43] J. Schwan, S. Ulrich, H. Roth, H. Ehrhardt, S.R.P. Silva, J. Robertson, R. Samlenski, R. Brenn, Tetrahedral amorphous carbon films prepared by magnetron sputtering and dc ion plating, *J. Appl. Phys.* 79 (1996) 1416–1422.